Beiträge aus der Elektrotechnik

Christoph Weimer

Characterization, Analysis, and Modeling of Dynamic Radio-Frequency Large-Signal Operating Limits, and Long-Term Reliability and Degradation of Silicon-Germanium Heterojunction Bipolar Transistors

Dresden 2025

Bibliografische Information der Deutschen Nationalbibliothek
Die Deutsche Nationalbibliothek verzeichnet diese Publikation in der Deutschen Nationalbibliografie; detaillierte bibliografische Daten sind im Internet über http://dnb.dnb.de abrufbar.

Bibliographic Information published by the Deutsche Nationalbibliothek
The Deutsche Nationalbibliothek lists this publication in the Deutsche Nationalbibliografie; detailed bibliographic data are available on the Internet at http://dnb.dnb.de.

Zugl.: Dresden, Techn. Univ., Diss., 2024

Die vorliegende Arbeit stimmt mit dem Original der Dissertation „Characterization, Analysis, and Modeling of Dynamic Radio-Frequency Large-Signal Operating Limits, and Long-Term Reliability and Degradation of Silicon-Germanium Heterojunction Bipolar Transistors“ von Christoph Weimer überein.

© Jörg Vogt Verlag 2025
Alle Rechte vorbehalten. All rights reserved.

Gesetzt vom Autor

ISBN 978-3-95947-077-3

Jörg Vogt Verlag
Niederwaldstr. 36
01277 Dresden
Germany

Phone: +49-(0)351-31403921
Telefax: +49-(0)351-31403918
e-mail: info@vogtverlag.de
Internet : www.vogtverlag.de

Technische Universität Dresden

Characterization, Analysis, and Modeling of Dynamic Radio-Frequency Large-Signal Operating Limits, and Long-Term Reliability and Degradation of Silicon-Germanium Heterojunction Bipolar Transistors

Dipl.-Ing. Christoph Weimer

der Fakultät Elektrotechnik und Informationstechnik der Technischen Universität Dresden

zur Erlangung des akademischen Grades eines

Doktoringenieurs

(Dr.-Ing.)

genehmigte Dissertation

Vorsitzender:	Prof. Dr.-Ing. habil. Thomas Zerna	Tag der Einreichung:	02. Mai 2024
Gutachter:	Prof. Dr.-Ing. habil. Michael Schröter	Tag der Verteidigung:	23. September 2024
Gutachter:	Prof. Dr. Tomislav Suligoj		
Weiteres Mitglied:	Prof. Dr. sc. techn. habil. Frank Ellinger		

Für Bodo, Angelika, Sebastian und Marta

Acknowledgments/Danksagung

The present thesis has been realized during my time as a researcher at the Chair for Electron Devices and Integrated Circuits at Technische Universität Dresden.

This work would not have been possible without the support, contributions, and also inspiration from my colleagues, friends, and family.

I would like to thank my supervisor, Prof. Michael Schröter, for offering me this research position, for his visions and constant support throughout the years, and for the freedom to develop my own ideas.

I would like to extend my appreciation to Prof. Tomislav Suligoj (University of Zagreb) for taking over the external review of this thesis.

I am thankful to the German National Science Foundation (Deutsche Forschungsgemeinschaft) for funding, which made this research possible. I am grateful to the IHP, in particular Dr. Gerhard Fischer, for the support, interest, and openness to research. I would also like to express my gratitude to Rohde & Schwarz for providing measurement equipment for my long-term experiments.

Additionally, I would like to thank all my colleagues. My office colleague, Dr. Eren Vardarli, provided helpful advice during power amplifier design, test chip design and also in the laboratory. Dr. Xiaodi Jin was a great collaborator in the laboratory and during the development of our automated layout generator. Mario Krattenmacher and Dr. Markus Müller offered helpful advice regarding HICUM/L2 and model parameter extraction. Viktor Kazantsev who had been recruited during my first year as teaching assistant became an excellent student researcher and contributed to this work. Dr. Paulius Sakalas gave me an initial introduction to the laboratory.

Ich danke Ria Lykowski für die Hilfestellung und Übernahme vieler administrativer Aufgaben. Lutz Hofmann danke ich für die Hilfestellung aller möglichen Art. Zudem danke ich Dr. Jörg Herricht für die angenehme Zusammenarbeit in der Lehre.

Von Herzen danke ich meinen Eltern Bodo und Angelika für die bedingungslose Unterstützung und die Ermöglichung dieses Bildungswegs, sowie meinem Bruder Sebastian. Ein besonderer Dank geht an meine Frau Marta für das Verständnis, die Unterstützung und die Geduld. Allen Freunden, die mich während der vergangenen Jahre begleitet haben, möchte ich danken. Dank gebührt auch der SG Dölzschen, da der Fußball immer ein hervorragender Ausgleich nach der harten Arbeit war.

Dresden, September 2024

Abstract

Silicon-Germanium (SiGe) heterojunction bipolar transistors (HBTs) are excellent candidates for radio frequency (RF) high power density applications due to their speed and drive capabilities. However, RF performance improvement of state-of-the-art high-speed SiGe HBTs inherently results in decreasing static breakdown voltages. This development raises concerns regarding safe operating limits and long-term reliability. In this context, the open-base collector-emitter breakdown voltage BV_{CEO} is a *static* figure of merit often specified by foundries in process design kits (PDKs) as an upper output voltage limit. This thesis addresses the limits of long-term RF operation and the characterization, analysis, and modeling of SiGe HBT degradation.

An automated load-pull setup is used to run RF stress tests under varying load conditions, and to periodically characterize DC and admittance parameters. Long-term RF stress tests at elevated RF output power density, implying large RF voltage and current density swings, demonstrate the reliable operability of SiGe HBTs far beyond conventional DC operating limits. Furthermore, the industry standard HBT compact model HICUM/L2 is shown to be an excellent vehicle for the exploration of extended operating regions of SiGe HBTs. RF operating limits are investigated. The physical cause of device degradation resulting from RF operation beyond these limits is analyzed. The understanding of extended RF operating limits is used and verified by the design, characterization, and stress tests of single-stage RF bipolar power amplifiers.

SiGe HBT degradation, which goes beyond a conventional I_B increase, causes an increase of the collector current I_C. This type of degradation is measurable only in RF operation at extremely elevated RF output power density. DC stress tests reveal that similar degradation does not result from strongly reverse-biased p-n junctions at low current densities, or elevated DC power densities at varying collector current densities. Degradation caused by RF stress is analyzed and modeled by means of the transfer saturation current. This enables the proposal of a modeling approach for the estimation of SiGe HBT degradation during RF operation. Numerical device simulation suggests that the I_C increase can be attributed to relaxation of compressive lattice strain in the base and its impact on the effective densities of states.

A comparative RF reliability study comprising a state-of-the-art SiGe HBT, an InP HBT and MOSFET technology is discussed. It reveals in particular that the BV_{CEO} of SiGe HBTs, which is lower than that of InP HBTs with similar RF performance, does not result in reduced RF reliability.

Kurzfassung

Silizium-Germanium-Heteroübergangs-Bipolartransistoren (SiGe HBTs) sind aufgrund ihrer Geschwindigkeit und Verstärkung ausgezeichnete Kandidaten für Hochfrequenzanwendungen (HF) mit hoher Leistungsdichte. Jedoch führt die Verbesserung der HF-Eigenschaften moderner SiGe HBTs zwangsläufig zu einer Verringerung der statischen Durchbruchspannungen. Daraus resultieren Bedenken hinsichtlich sicherer Betriebsgrenzen und langfristiger Zuverlässigkeit. In diesem Zusammenhang ist die mit offener Basisklemme gemessene Kollektor-Emitter-Durchbruchspannung BV_{CEO} eine *statische* Kenngröße, die häufig von Halbleiterherstellern in Prozess-Design-Kits (PDKs) als obere Ausgangsspannungsgrenze angegeben wird. Diese Arbeit thematisiert die Grenzen des langfristigen *dynamischen* HF-Betriebs, sowie die Charakterisierung, Analyse und Modellierung der Degradation moderner SiGe HBTs.

Ein automatisierter *Load-Pull*-Aufbau ermöglicht die Durchführung dynamischer Stresstests unter variablen Lastbedingungen bei regelmäßiger Charakterisierung von DC- und Kleinsignal-Parametern. Langzeitbetrieb bei erhöhter HF-Ausgangsleistungsdichte belegt die zuverlässige Funktionsfähigkeit von SiGe HBTs weit über herkömmliche DC-Betriebsgrenzen hinaus. Zudem wird die Eignung des HBT-Kompaktmodells HICUM/L2 für die Erschließung erweiterter Betriebsbereiche von SiGe HBTs demonstriert. HF-Betriebsgrenzen werden untersucht. Die physikalische Ursache der Degradation, die bei HF-Betrieb über diese Grenzen hinaus resultiert, wird analysiert. Das Verständnis erweiterter HF-Betriebsgrenzen wird durch den Entwurf, die Charakterisierung und Belastungstests bipolarer HF-Leistungsverstärker genutzt und verifiziert.

Über den herkömmlichen I_{B}-Anstieg hinausgehende Degradation von SiGe HBTs erwirkt einen Anstieg des Kollektorstroms I_{C}. Diese ist nur im HF-Betrieb bei extrem erhöhter HF-Ausgangsleistungsdichte messbar. DC-Stresstests zeigen, dass diese Art der Degradation nicht durch erhöhte DC-Leistungsdichten bei unterschiedlichen Kollektorstromdichten verursacht wird. Auch wird sie nicht durch stark sperrgepolte pn-Übergänge bei niedrigen Stromdichten verursacht. Die durch HF-Stress verursachte Degradation wird anhand des Transfer-Sättigungsstroms analysiert und modelliert. Dies ermöglicht die Formulierung eines Modellierungsansatzes zur Abschätzung der Degradation während des HF-Betriebs. Numerische Simulationen legen nahe, dass der I_{C}-Anstieg auf die Relaxation der kompressiven Gitterspannung in der Basis und deren Einfluss auf die effektiven Zustandsdichten zurückzuführen ist.

Es wird eine vergleichende HF-Zuverlässigkeitsstudie diskutiert, die eine moderne SiGe HBT-, InP HBT- und MOSFET-Technologie umfasst. Es wird insbesondere gezeigt, dass das BV_{CEO} von SiGe HBTs, das niedriger ist als das von InP HBTs mit vergleichbaren HF-Eigenschaften, nicht zu einer verringerten HF-Zuverlässigkeit führt.

CONTENTS

List of Symbols **xii**

1 Introduction **1**

2 Si BJT and SiGe HBT reliability fundamentals **15**
2.1 Literature overview 16
2.2 The physics of the reverse-biased p-n junction 17
2.2.1 Selected stress methodologies reported in the literature 17
2.2.2 Band-to-band tunneling current density in reverse-biased BE junction 21
2.2.3 Low-injection avalanche current density in reverse-biased BC junction 23
2.2.4 DC stress with strongly reverse-biased BC and BE junction . . 23
2.3 Shockley-Read-Hall recombination current density 25
2.4 Analytical load ellipse calculation 30
2.5 Ground-signal-ground layout and probes 35

3 RF reliability investigations with a passive load-pull setup **39**
3.1 RF large-signal transistor characterization with load tuning 39
3.2 Load-pull setup: characterization and calibration 41
3.2.1 Setup description 41
3.2.2 Measurement reproducibility 43
3.2.3 Calculation and modeling of the load impedance 45
3.2.4 Power delivered to the load 50
3.2.5 Power calibration 50
3.3 SiGe HBT characterization in extended RF operating regions using load-pull 52
3.4 DC and RF stress test 59

4 Characterization of SiGe HBT degradation caused by RF operation **65**
4.1 RF large-signal transistor characterization with load and source tuning 65
4.2 DC, small-signal and large-signal device characterization 67
4.3 RF stress test 73

5 Analysis and modeling of degradation physics for RF circuit design 77
5.1 DC stress tests at elevated static power densities 78
5.2 RF stress tests of SiGe HBTs with varying emitter widths 83
5.2.1 Long-term RF stress at maximum power-added efficiency . . 84
5.2.2 Long-term RF stress for degradation acceleration: die I 86
5.2.3 Long-term RF stress for degradation acceleration: die II . . . 88
5.2.4 Measurement data analysis 90
5.3 Analysis of the cause of degradation resulting from RF stress 97
5.3.1 Analysis with HICUM/L2 97
5.3.2 Analytical modeling of degradation in dependence on RF output power density 101
5.3.3 Numerical device simulation aided phenomenological study . 104
5.3.4 Investigation of the temperature effect on the transfer saturation current density before and after RF stress using measurements and TCAD 110

6 Frequency-dependent RF stress tests with terminated and open output 115
6.1 DC, small-signal and large-signal device characterization 117
6.2 RF stress tests of DUTs in GSG layout 122
6.2.1 RF stress test with terminated output 122
6.2.2 RF stress test with open output 126
6.2.3 Analysis, discussion and conclusion 132
6.3 RF stress tests of power amplifiers 140
6.3.1 Power amplifier basics 140
6.3.2 60-GHz single-stage power amplifier 143
6.3.2.1 Power amplifier characterization 145
6.3.2.2 RF stress test 147
6.3.3 90-GHz single-stage power amplifier 149
6.3.3.1 Power amplifier characterization 150
6.3.3.2 RF stress test 153

7 Comparative RF reliability study across transistor process technologies 155
7.1 Silicon-Germanium HBT process B11HFC (Infineon) 164
7.1.1 RF large-signal device characterization 164
7.1.2 RF stress tests 168
7.1.2.1 RF stress test: die I 168
7.1.2.2 RF stress test: die II 170
7.2 Indium-Phosphide HBT process TSC250 (Teledyne) 171
7.2.1 RF large-signal device characterization 171
7.2.2 RF stress tests 178
7.2.2.1 RF stress test: die I 178
7.2.2.2 RF stress test: die II 180

7.3 Fully depleted SOI MOSFET process 22FDX (Globalfoundries) . . . 181
7.3.1 RF large-signal device characterization 181
7.3.2 DC and RF stress tests 186
7.3.2.1 DC and RF stress test: die I 186
7.3.2.2 DC stress test: die II 187
7.3.2.3 DC stress test: die III 188
7.3.2.4 DC and RF stress test: die IV 189
7.3.2.5 RF stress test: die V 190
7.3.2.6 Conclusion 191

8 Summary, conclusion and outlook 193

A Complementary experimental data 199
A.1 Complements to chapter 4 199
A.2 Complements to chapter 5 200
A.2.1 Measurements after RF stress at maximum power-added efficiency 200
A.2.2 Measurements after RF stress for different emitter geometries 202
A.2.3 Time-dependent degradation 207
A.2.4 Periodic capacitance measurements 209
A.3 Complements to chapter 6 210
A.4 Complements to chapter 7 211
A.4.1 B11HFC, time-dependent degradation 212
A.4.2 TSC250, RF stress tests 214
A.4.2.1 RF stress test: die I 214
A.4.2.2 RF stress test: die II 215
A.4.3 22FDX, measurements after DC stress 216
A.4.4 22FDX, measurements after RF stress 217

B Mathematics and semiconductor device physics 219
B.1 Tunneling current density 219
B.2 Shockley-Read-Hall recombination 221
B.3 Maxwell velocity distribution 222
B.4 Inverse Fourier transformation 223
B.5 Static collector current in large-signal dynamic operation 223
B.6 Principal axis theorem 224
B.7 Two-port parameter conversions 226

Bibliography 229

List of Symbols

Physical Constants

h	Planck constant	$6.626 \cdot 10^{-34}\,\mathrm{J\,s}$, $4.136 \cdot 10^{-15}\,\mathrm{eV\,s}$
$\hbar = h/(2\pi)$	Reduced Planck constant	$1.055 \cdot 10^{-34}\,\mathrm{J\,s}$, $6.582 \cdot 10^{-16}\,\mathrm{eV\,s}$
k_B	Boltzmann constant	$1.381 \cdot 10^{-23}\,\mathrm{J/K}$, $8.617 \cdot 10^{-5}\,\mathrm{eV/K}$
q	Elementary charge	$1.602 \cdot 10^{-19}\,\mathrm{A\,s}$
ε_0	Absolute permittivity	$8.854 \cdot 10^{-12}\,\mathrm{A\,s/(V\,m)}$

Mathematical notations

j	Imaginary unit, $\mathrm{j}^2 = -1$
x	Real-valued variable
$\lvert x \rvert$	Absolute value of x
$x \propto y$	x proportional to y
$\underline{x}$	Complex-valued variable
$\mathrm{Re}\{\underline{x}\}$, $\mathrm{Im}\{\underline{x}\}$	Real, imaginary part of complex-valued variable
$\vec{x}$, $[x]$	Vector, matrix containing real-valued entries
$\vec{\underline{x}}$, $[\underline{x}]$	Vector, matrix containing complex-valued entries
$\vec{x}^\top$, $[x]^\top$	Transpose of a vector matrix
$\exp(x)$	Exponential function $\exp(x) = \mathrm{e}^x$, $\mathrm{e} = 2.71828\ldots$
$\sinh(x)$	Hyperbolic sine, $\sinh(x) = \frac{1}{2}\left(\mathrm{e}^x - \mathrm{e}^{-x}\right)$
$\cosh(x)$	Hyperbolic cosine, $\cosh(x) = \frac{1}{2}\left(\mathrm{e}^x + \mathrm{e}^{-x}\right)$
$\log(x)$	Common logarithm with base 10, $\log(x) = \log_{10}(x)$
$\det[x]$	Determinant of matrix $[x]$
$\delta(x)$	Relative deviation of $x(t)$ with respect to initial value $x(t=0)$, defined in (1.7)
Δx	Difference

Latin variables

Variable	Unit	Description
A_{E0}	$\mathrm{m^2}$	Emitter window area
b_{E0}	m	Emitter window width
B_{f}	-	DC forward current gain
BV_{CEO}	V	Open-base collector-emitter breakdown voltage
BV_{CBO}	V	Open-emitter collector-base breakdown voltage
BV_{EBO}	V	Open-collector emitter-base breakdown voltage
c_{10}	$\mathrm{A^2\,s}$	GICCR constant
C, C_{BE}, C_{BC}	F	Electrical capacitance, BE and BC capacitance
C_{jEi0}, C_{jCi0}	F	Internal zero-bias BE and BC junction capacitance
C_{mat}	-	Material composition grading
$\mathscr{C}_{\mathrm{th}}$	$\mathrm{W\,s/K}$	Thermal capacitance
E	$\mathrm{V/m}$	Electric field
f, f_0	Hz	Frequency, fundamental frequency
f_{T}, $f_{\mathrm{T,peak}}$	Hz	Transit/cut-off frequency, peak transit frequency
f_{max}	Hz	Maximum oscillation frequency
f_{avl}	$1/\mathrm{V}$	Avalanche current factor
FLSH	-	Flag to turn self-heating effect on and off (see [132])
G_{t}	-	Transducer power gain
$G_{\mathrm{T,max}}$	-	Maximum available gain
$\lvert \underline{H}_{21} \rvert$	-	Absolute value of small-signal current gain
I_{AVL}, I_{T}	A	Static avalanche, transfer current
I_{REpS}	A	Peripheral BE recombination saturation current
IL	-	Insertion loss
J_i, j_i	$\mathrm{A/m^2}$	Static, dynamic current density into the node $i \in \{\mathrm{B,C,E}\}$ for an HBT, $i \in \{\mathrm{G,D,S}\}$ for a MOSFET
$J_{\mathrm{C,peak}-f_{\mathrm{T}}}$	$\mathrm{A/m^2}$	Collector current density at peak-f_{T}
$J_{\mathrm{C,peak}-f_{\mathrm{max}}}$	$\mathrm{A/m^2}$	Collector current density at peak-f_{max}
$J_{\mathrm{C,q}}$	$\mathrm{A/m^2}$	Quiescent collector current density
J_{t}	$\mathrm{A/m^2}$	Static tunneling current density
J_{rg}	$\mathrm{A/m^2}$	Recombination-generation current density
K	-	Rollet's stability factor
l_{E0}	m	Emitter window length
L	H	Inductance

m^*	kg	Effective mass
m	-	Ideality factor
m_{REp}	-	Peripheral BE recombination current ideality factor
$\vec{M}$	-	Tuner motor position
n, n_{i}	$1/\text{m}^3$	Electron density, intrinsic carrier density
n_{iB}	$1/\text{m}^3$	Intrinsic carrier density in the base region
N_{D}, N_{A}	$1/\text{m}^3$	Concentrations of donors, acceptors
N_{C}	$1/\text{m}^3$	Effective density of states in the conduction band
N_{V}	$1/\text{m}^3$	Effective density of states in the valence band
N_{tr}	$1/\text{m}^3$	Volumetric trap density
N_x	-	Number of emitter fingers
p	$1/\text{m}^3$	Hole density
p_x, $p_\perp$	$\text{kg}\,\text{m}/\text{s}$	Momentum in x-direction, perpendicular momentum
P_{E0}	m	Emitter window perimeter
$P_{\text{L,del}}$	W	Power delivered to the load by a transistor (DUT) at f_0
$P_{\text{L,del,PA}}$	W	Power delivered to the load by a power amplifier at f_0
P_{avs}	W	Power available from the source
P_{DC}	W	DC power consumption
PAE	-	Power-added efficiency
PAE_{max}	-	Power-added efficiency peak value
r_{SRH}	$1/(\text{m}^3\,\text{s})$	SRH recombination rate
R	Ω	Electrical resistance
$\mathscr{R}_{\text{th}}$	K/W	Thermal resistance
$\underline{S}_{ij}$	-	Scattering parameter for the terminals $i, j \in \{1,2\}$
t, t_{wait}, t_{stress}	s	Time, waiting time, stress time
T, T_{B}	K	Temperature, chuck/die back-side temperature
T_{j}	K	Junction temperature
$\underline{T}_{ij}$	-	Chain scattering parameter for the terminals $i, j \in \{1,2\}$
U	-	Unilateral power gain
$V_{\text{g}} = W_{\text{g}}/q$	V	Bandgap voltage
$V_T = k_{\text{B}}T/q$	V	Thermal voltage
V_{knee}, V_{max}, V_{op}	V	Knee, maximum, operating point voltage
V_{bi}, V_{r}	V	Built-in, reverse-bias voltage of a p-n junction
V_{nom}	V	Nominal voltage of a MOSFET process

V_{ij}, v_{ij}	V	Static, dynamic voltage between the nodes $i, j \in \{B, C, E = S\}$ for HBTs and $i, j \in \{G, D, S = B\}$ for MOSFETs
V_{BB}, V_{CC}	V	Input, output supply voltage of power amplifier
w	m	Width (of a SCR)
W_G, $W_{G,eff}$	m	Gate width, effective gate width
W, W_V, W_C	W s	Energy, valence band energy, conduction band energy
W_{tr}	W s	Trap energy
W_g, W_F	W s	Bandgap energy, Fermi energy
W_{Fp}, W_{Fn}	W s	Quasi-Fermi energy of p-side, n-side in a p-n junction
$\underline{Y}_{ij}$	S	Admittance parameter for the terminals $i, j \in \{1, 2\}$
$\underline{Z}_L$, $\underline{Z}_S$	Ω	Load, source impedance
$\underline{Z}_{ij}$	Ω	Impedance parameter for the terminals $i, j \in \{1, 2\}$
Z_0	Ω	Characteristic impedance of transmission line
$\underline{\mathscr{Z}}_{th}$	K/W	Thermal impedance

Greek variables

Variable	**Unit**	**Description**
$\underline{\Gamma}_L$, $\underline{\Gamma}_S$	-	Load, source reflection coefficient
$\underline{\Gamma}_{L0} = \underline{\Gamma}_L\|_{f_0}$	-	Load reflection coefficient at the fundamental frequency f_0
$\Delta T_j = T_j - T_B$	K	Junction temperature increase
θ	°	Electrical length
λ	m	Wavelength
μ, μ_{nB}	$m^2/(V\,s)$	Mobility, electron mobility in the base region
$\rho_{L,del}$	-	Logarithmic RF output power density (per area) of an HBT, defined in (1.8)
$\sigma_{L,del}$	-	Logarithmic RF output power density (per length) of an HBT and a MOSFET, defined in (1.9) and (1.10)
τ_{th}	s	Thermal time constant
τ_{stress}	s	Stress time constant
φ_n, φ_p	V	Quasi-Fermi potential for electrons, holes
ψ	V	Electrostatic potential
$\omega = 2\pi f$	Hz	Angular frequency

Acronyms

AC	Alternating current
Al	Aluminum
Au	Gold
B	Base
BEOL	Backend-of-line
BiCMOS	Bipolar and complementary metal oxide semiconductor
BJT	Bipolar junction transistor
C	Collector
CMOS	Complementary metal oxide semiconductor
Cu	Copper
DC	Direct current
DOS	Density of states
DUT	Device under test
E	Emitter
EM	Electromagnetic(ally)
FD	Fully depleted
Ge	Germanium
GICCR	Generalized integral charge-control relation
GPG	Ground-power-ground
GSG	Ground-signal-ground
HBT	Heterojunction bipolar transistor
HICUM/L2	High-current model/level2
IHP	Innovations for High Performance Microelectronics
	Leibniz-Institut für innovative Mikroelektronik
InP	Indium-Phosphide
LP	Load-pull
LS	Large-signal
MOSFET	Metal-oxide-semiconductor field-effect transistor
OP	Operating point
PA	Power amplifier
PDK	Process design kit
RF	Radio frequency
SCR	Space charge region
SCPI	Standard commands for programmable instruments

SEM	Scanning electron microscopy
Si	Silicon
SiGe	Silicon-Germanium
SMU	Source measure unit
SOA	Safe operating area
SOI	Silicon on insulator
SRH	Shockley-Read-Hall
STEM	Scanning transmission electron microscopy
TCAD	Technology computer-aided design
TEM	Transmission electron microscopy
TL	Transmission line
VNA	Vector network analyzer

CHAPTER 1

INTRODUCTION

SILICON-GERMANIUM (SiGe) heterojunction bipolar transistors (HBTs) and their integration with high-density complementary metal-oxide-semiconductor (CMOS) processes are excellent candidates for radio frequency (RF) high power density applications. They leverage the mature manufacturing tools of CMOS with the speed and drive capabilities of SiGe HBTs, e.g., [25, 70, 125, 133, 141].

To achieve the maximum possible RF output power density, large current density and voltage swings are required. RF performance improvement of SiGe HBTs, i.e., higher peak cut-off frequency $f_{\mathrm{T,peak}}$, requires an increasing collector doping concentration to alleviate high-current effects [74, 135]. This inherently results in decreasing static breakdown voltages [69], thus posing the question of transistor safe operating limits and reliability. In this context, the open-base collector-emitter (CE) breakdown voltage BV_{CEO} is a *static* figure of merit often specified by foundries in process design kits (PDKs) as an upper output voltage limit.

Conventionally, SiGe HBT operating limits have been experimentally explored by applying direct-current (DC) stress to the device under test (DUT) *(i)* through a strongly reverse-biased base-emitter (BE) junction, or *(ii)* in bias points where $V_{\mathrm{CE}} > BV_{\mathrm{CEO}}$ causes a high collector-base (CB) voltage V_{CB} at different collector current density levels J_{C} [35, 172]. Moreover, for the purpose of characterizing device degradation, the research focus has been on the low-injection DC base current increase due to traps generated in the emitter perimeter region [27, 28].

This conventional methodology, consisting of DC stress and subsequent characterization of the DC base current degradation, does not fully explore SiGe HBT operating limits for two reasons. Firstly, *static* operating limits are not the same as *dynamic* large-signal (LS) operating limits because physical breakdown phenomena, which lead to device destruction in DC operation, e.g., thermal runaway, are significantly diminished or even entirely suppressed during fast transient RF signal swings. Secondly, the DC base current I_B, especially at low injection levels, is only of little relevance to many analog RF circuit blocks, in particular power amplifiers and driver circuits, and hence an unsatisfactory indicator of RF device reliability and degradation. Given this rationale, the actual *RF operating limits* lie beyond statically determined DC operating limits, thus making RF stress tests indispensable for the characterization of SiGe HBT robustness and long-term reliability for RF large-signal circuit applications.

The aim of this work is to extend the understanding of SiGe HBT reliability and to obtain a more complete picture of device degradation by applying various stress techniques to state-of-the-art SiGe HBTs. These techniques include:

(i) DC stress tests with strongly reverse-biased BE and BC junction at low injection levels to investigate degradation driven by the electric field,

(ii) DC stress tests at elevated J_C at low to high V_CE to characterize degradation driven by the current density at different junction temperatures,

(iii) RF stress tests to characterize and systematically analyze device degradation driven by RF large-signal operation.

Special emphasis is placed on *long-term* reliability experiments with typical stress test durations in the range $300\,\mathrm{h} \ldots 1200\,\mathrm{h}$. By experimentally demonstrating the (RF) robustness of SiGe HBTs, this work also aims at motivating semiconductor manufacturers to revise their device operating limits specifications.

In order to investigate degradation in this work, the long-term stress tests are periodically interrupted to measure small-signal parameters in addition to DC characteristics. In particular admittance parameters are more important for RF circuit design than the DC base current, as they enable the attribution of possible degradation-related changes to conductances and capacitances associated with the transistor structure. An experimental load-pull setup, fully automated in Python to carry out RF LS stress tests and periodic measurements of small-signal parameters, is presented in this thesis and discussed along with concepts relevant to long-term reliability tests.

Throughout this thesis, the industry standard HBT compact model HICUM/L2 [134, 136] is used within a Python-based object-oriented toolkit [5, 76]. The HICUM/L2 equivalent circuit is shown in Fig. 1.1a with the intrinsic transistor given in Fig. 1.1b. Large-signal measurements and simulations in extended RF operating regions using various high-speed HBT process technologies demonstrate the suitability and accuracy of HICUM/L2 for the exploration of dynamic HBT operating limits. Such investigations complement previous studies, e.g., [130, 137, 138].

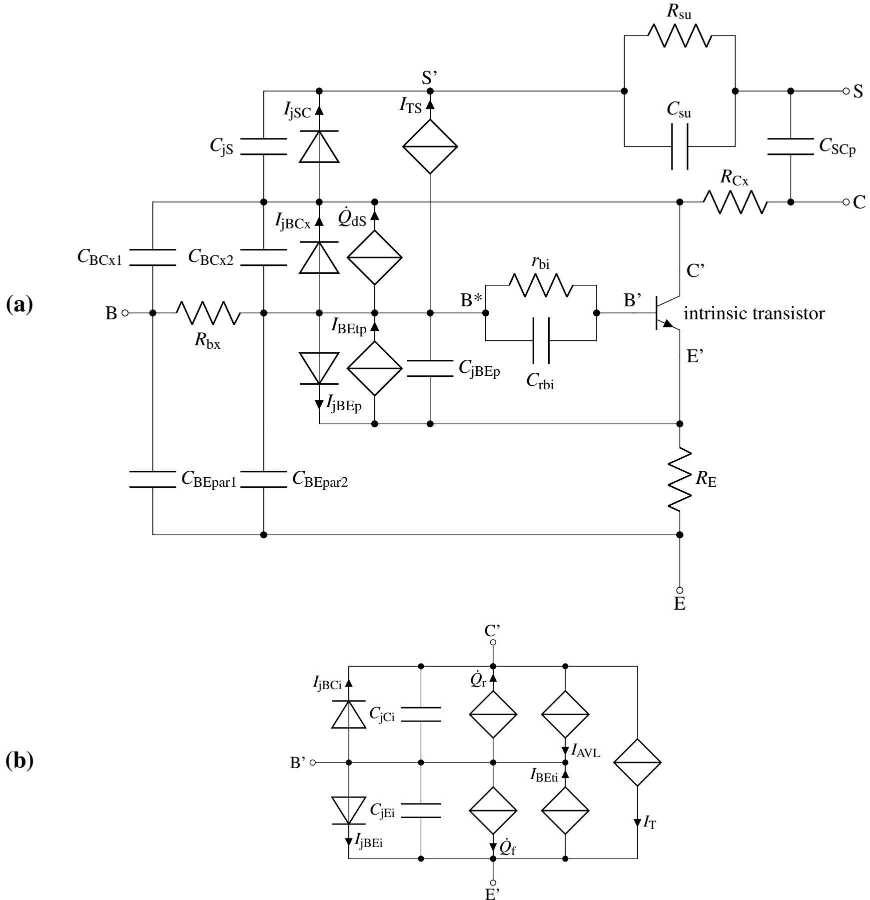

Figure 1.1: **(a)** HICUM/L2 equivalent circuit with **(b)** intrinsic transistor; (adjunct) networks for substrate coupling, noise correlation, self-heating and non-quasi-static effects [134, 136] are not shown.

Previous approaches to modeling the degradation-caused increase of the DC I_B have focused on the peripheral BE recombination saturation current I_{REpS} [96, 167]. This HICUM/L2 parameter has been chosen for the modeling of I_B degradation because it

can be physically related to traps peripherally located at the emitter-base spacer oxide, as discussed in Sec. 2.3 of this thesis. To advance the state of the art, the explicit goal of this work is to characterize degradation caused by RF LS stress beyond a low-injection DC I_B increase and to employ HICUM/L2 in order to understand degradation beyond I_{REpS}. Building upon a sound experimental basis, the aim is to propose and to initiate the development of an analytical expression for the estimation of SiGe HBT degradation during RF circuit design. This work aims at initiating systematic research on SiGe HBT degradation caused by RF stress, with the intention of providing a clear direction for future research to be pursued by semiconductor foundries.

Thesis structure. Usually, a typical scientific approach to problem-solving consists of verifying the assumptions of a known theory first, which is then applied to experimental data in practice. RF reliability works the other way around, as no theory exists whatsoever concerning the physics of SiGe HBT degradation caused by RF stress. In reliability research, a theory can only be derived from experimental insights. The degradation of I_B typically investigated in the literature represents only a fraction of the broader picture. Thus significant work remains to be done regarding the investigation of degradation of all HBT characteristics. Consequently, this thesis has a strong experimental focus and is subdivided into eight chapters. Note that the investigated process technology of this chapter and of Ch. 2 - 6 is IHP's state-of-the-art high-speed SiGe HBT technology SG13G2 [50]. Ch. 2 provides Si BJT and SiGe HBT reliability basics, including the physics of the reverse-biased p-n junction and electromigration investigations on the backend-of-line. Ch. 3 and 4 present a passive load-pull setup and related theory, large-signal measurements and simulations, as well as DC and RF stress tests revealing a new type of degradation. Ch. 5 discusses thorough RF reliability investigations for DUTs with scalable emitter window dimensions in CBEBC contact configuration, as well as an analysis using HICUM/L2 and numerical device simulation. Ch. 6 discusses RF stress tests under specific load conditions for DUTs with BEC contacts. Furthermore, in Ch. 6 the understanding of extended RF operating limits of SiGe HBTs is verified and corroborated by the design, characterization and stress tests of single-stage RF bipolar power amplifiers. Moreover, the comparative study in Ch. 7 investigates the particular challenges related to RF reliability of different state-of-the-art transistor process technologies: Infineon's SiGe HBT technology B11HFC [12], Teledyne's Indium-Phosphide (InP) HBT technology TSC250 [151] and Globalfoundries' MOSFET technology 22FDX [16, 109]. Lastly, Ch. 8 summarizes this work, draws final conclusions and provides an outlook for future research.

Static bipolar transistor breakdown voltages. The static breakdown voltages of the SiGe HBT technology SG13G2 are subsequently recapitulated. They are referenced when defining the static and dynamic stress conditions of the long-term reliability tests discussed in this thesis. An illustration and experimental determination of the breakdown voltages are given in Fig. 1.2.

Open-base collector-emitter breakdown voltage. The open-base collector-emitter breakdown voltage BV_{CEO}, illustrated in Fig. 1.2a, is defined and practically meaningful for a forced $I_{\mathrm{B}} = \mathrm{const.}$ corresponding to a large source resistance. Under such bias conditions, as shown in Fig. 1.2b, a significant increase of J_{C} can be observed for $V_{\mathrm{CE}} > BV_{\mathrm{CEO}}$ because holes, generated by impact ionization in the BC space charge region, are back-injected into the emitter, thus causing an amplification of the avalanche current by the DC forward current gain B_{f}.

In practice, BV_{CEO} is often defined with a relatively low forced V_{BE} in such a way that the mobile electron density is significantly lower than the collector doping concentration. With forced V_{BE} corresponding to a relatively high transistor input impedance, impact-ionization-generated holes can flow out of the base terminal and hence eventually overcompensate the forward base current, resulting in what is commonly referred to as base current reversal [84]. The V_{CE}, at which this base current reversal occurs at $V_{\mathrm{BE}} = \mathrm{const.}$, is BV_{CEO} and, as shown in Fig. 1.2b, closely corresponds to the maximum V_{CE} prior to the significant J_{C} increase at $I_{\mathrm{B}} = \mathrm{const.}$ For the SiGe HBT process technology SG13G2 is $BV_{\mathrm{CEO}} \approx 1.6\,\mathrm{V}$.

Open-emitter collector-base breakdown voltage. The open-emitter collector-base breakdown voltage BV_{CBO} related to the BC junction (cf. Fig. 1.2c) is approximated here at $V_{\mathrm{BE}} = 0$ because the DUT is embedded in a ground-signal-ground (GSG) layout with grounded emitter. As shown in Fig. 1.2d the V_{CB}, at which the slope $\mathrm{d}J_{\mathrm{C}}/\mathrm{d}V_{\mathrm{CB}}$ significantly increases, closely corresponds to $BV_{\mathrm{CBO}} \approx 4.8\,\mathrm{V}$ specified in the PDK (defined at $I_{\mathrm{E}} = 0$, $J_{\mathrm{C}} = 0.83\,\mu\mathrm{A}/\mu\mathrm{m}^2$ for a device with $A_{\mathrm{E0}} = 0.12\,\mu\mathrm{m}^2$).

Open-collector emitter-base breakdown voltage. The open-collector EB breakdown voltage BV_{EBO} related to the BE junction (cf. Fig. 1.2e) is obtained at $I_{\mathrm{C}} = 0$. As shown in Fig. 1.2f the V_{EB}, at which the slope $\mathrm{d}J_{\mathrm{E}}/\mathrm{d}V_{\mathrm{EB}}$ significantly increases, closely corresponds to $BV_{\mathrm{EBO}} \approx 1.6\,\mathrm{V}$ specified in the PDK (defined at $I_{\mathrm{C}} = 0$, $J_{\mathrm{E}} = 8.3\,\mu\mathrm{A}/\mu\mathrm{m}^2$ for a device with $A_{\mathrm{E0}} = 0.12\,\mu\mathrm{m}^2$).

The $J_{\mathrm{C}}(V_{\mathrm{CB}})$ increase in Fig. 1.2d and eventual breakdown of the BC junction are caused by avalanche multiplication, whereas the $J_{\mathrm{E}}(V_{\mathrm{EB}})$ increase in Fig. 1.2f and eventual breakdown of the BE junction are caused by tunneling [134].

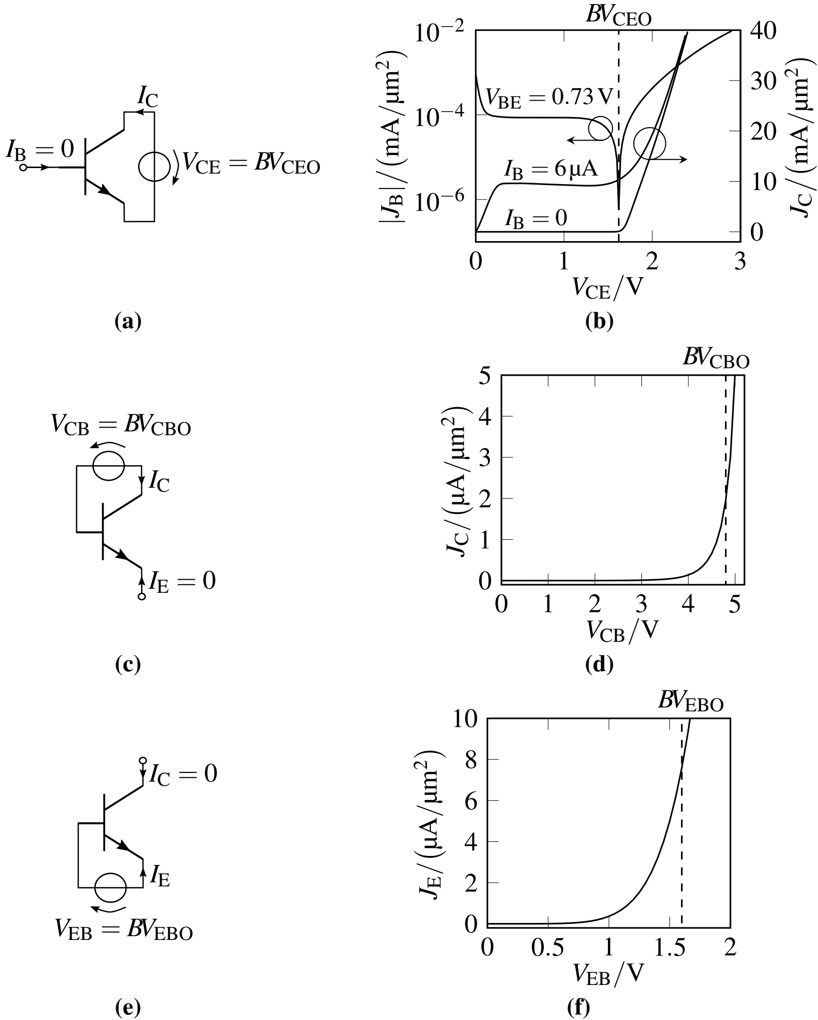

Figure 1.2: Illustration of the original definition of **(a)** the open-base collector-emitter breakdown voltage BV_{CEO} **(c)** the open-emitter collector-base breakdown voltage BV_{CBO} **(e)** the open-collector emitter-base breakdown voltage BV_{EBO}. Experimental determination of **(b)** $BV_{CEO} \approx 1.6\,V$ at $I_B/\mu A = \{0.0, 6.0\}$ and $V_{BE} = 0.73\,V$ **(d)** $BV_{CBO} \approx 4.8\,V$ approximated at $V_{BE} = 0$ **(f)** $BV_{EBO} \approx 1.6\,V$ at $I_C = 0$. The emitter window of the DUT has the dimension $b_{E0} = 0.12\,\mu m$, $l_{E0} = 2.65\,\mu m$. © IEEE [166].

Johnson Limit. The semiconductor material of a bipolar transistor "has a maximum capability for energizing electric charges that process a signal" [69]. If all other contributions are neglected, the time τ required for carriers to traverse the drift region of length l needs to be reduced to increase the cut-off frequency $f_T = 1/(2\pi\tau)$. This can be realized by increasing the voltage drop V across the drift region, resulting in a higher electric field V/l and an increased carrier drift velocity. If these charge carriers reach the material-specific saturated drift velocity v_s, the time τ can be reduced even further by decreasing the distance l. However, this increases the electric field V/l, which eventually reaches a limiting dielectric breakdown field $E_{lim} = V_{lim}/l$. Hence the limit $v_s\tau = V_{lim}/E_{lim}$ is deduced [69]. Based on these simplified considerations, a material-specific relation between maximum voltage V_{lim} and cut-off frequency $f_{T,peak}$, commonly known as the *Johnson Limit*, is provided [69]

$$V_{lim} f_{T,peak} = \frac{E_{lim} v_s}{2\pi} = \begin{cases} 2 \cdot 10^{11}\,\mathrm{V/s} & \text{Silicon,} \\ 1 \cdot 10^{11}\,\mathrm{V/s} & \text{Germanium.} \end{cases} \tag{1.1}$$

The oversimplifications of these numbers are discussed in [106] for Si BJTs and in [141] for SiGe HBTs. For a realistic perspective, a relation $BV_{CEO}(f_{T,peak})$ is illustrated in Fig. 1.3 which reviews various SiGe HBT process technology generations. The hyperbolic numerical fit in Fig. 1.3 contains a constant offset value. This can be attributed to considerable RF performance improvement, e.g., from IHP's SG13G2 process with $f_{T,peak} = 300\,\mathrm{GHz}$ [50] to its successor SG13G3 with $f_{T,peak} = 505\,\mathrm{GHz}$ [52], achieved without compromising BV_{CEO}.

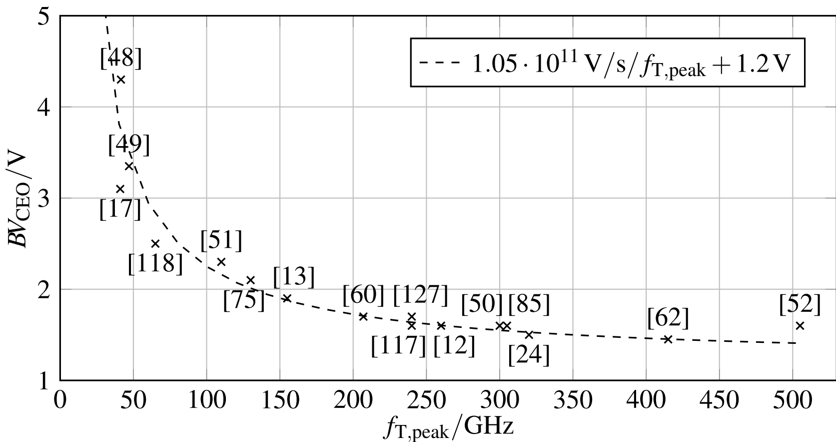

Figure 1.3: Illustration of the trade-off between high breakdown voltage BV_{CEO} and high peak cut-off frequency $f_{T,peak}$ at room temperature reviewing various SiGe HBT process technology generations. The dashed line represents a fit.

Breakdown effects in dynamic transistor operation. When evaluating device reliability under RF LS operating conditions, it is important to consider the dynamic behavior of physical breakdown phenomena. Self-heating is a major reliability concern for SiGe HBTs. Fig. 1.4 depicts the absolute value of the thermal impedance $|\underline{\mathscr{Z}}_{\mathrm{th}}|$ as a function of frequency in different operating points. $|\underline{\mathscr{Z}}_{\mathrm{th}}|$ has been characterized by applying the admittance parameter method [83] to the technology SG13G2. More details on the characterization are reported in [67]. Fig. 1.4 demonstrates that $|\underline{\mathscr{Z}}_{\mathrm{th}}|$ tends to zero for practical operating frequencies which are typically larger than 1 GHz for modern SiGe high-speed technologies.

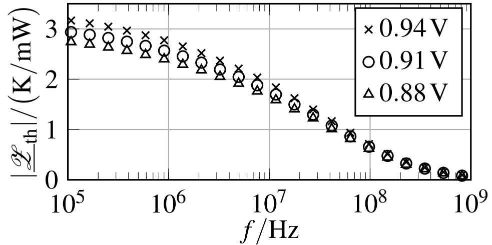

Figure 1.4: Frequency-dependent characterization of the absolute value of the thermal impedance $\underline{\mathscr{Z}}_{\mathrm{th}}$ of a SiGe HBT from the process SG13G2 using the admittance parameter method [83]. The legends specify V_{BE} values. The data were obtained at $T_{\mathrm{B}} = 323\,\mathrm{K}$ and $V_{\mathrm{CE}} = 0.75\,\mathrm{V}$. © IEEE [166].

Considering the self-heating modeling with an adjunct single-pole network implemented in many compact models, the frequency-dependent relation $\underline{\mathscr{Z}}_{\mathrm{th}}(f)$ reads

$$\underline{\mathscr{Z}}_{\mathrm{th}} = \frac{\mathscr{R}_{\mathrm{th}}}{1 + \mathrm{j}2\pi\tau_{\mathrm{th}}f} \tag{1.2}$$

with the thermal resistance $\mathscr{R}_{\mathrm{th}}$, the thermal time constant $\tau_{\mathrm{th}} = \mathscr{R}_{\mathrm{th}}\mathscr{C}_{\mathrm{th}}$ and the thermal capacitance $\mathscr{C}_{\mathrm{th}}$. If the period duration $T = 1/f$ becomes significantly smaller than the thermal time constant τ_{th}, i.e., $\tau_{\mathrm{th}} \gg T$, self-heating cannot follow the dynamic signal swings anymore and for the absolute value of $\underline{\mathscr{Z}}_{\mathrm{th}}$ follows

$$|\underline{\mathscr{Z}}_{\mathrm{th}}| = \frac{\mathscr{R}_{\mathrm{th}}}{\sqrt{1 + 4\pi^2(\tau_{\mathrm{th}}/T)^2}} \xrightarrow{\tau_{\mathrm{th}} \gg T} 0. \tag{1.3}$$

Hence, self-heating is only relevant when choosing the quiescent operating point[1], but is no practical concern for dynamic LS swings. In other words, the very phenomenon that causes breakdown in DC operation is significantly diminished or even entirely suppressed in RF operation. This rationale suggests that the maximum permissible CE voltage is different depending on whether quiescent V_{CE} or transient $v_{\mathrm{CE}}(t)$ are considered. An efficient and practical way to visualize and quantify this difference is to examine output characteristics with and without self-heating using HICUM/L2.

[1] Note that the tautology of terms like *quiescent operating point*, *RF frequency* or *DC bias* is intentionally used throughout this thesis given the technical clarity of these terms.

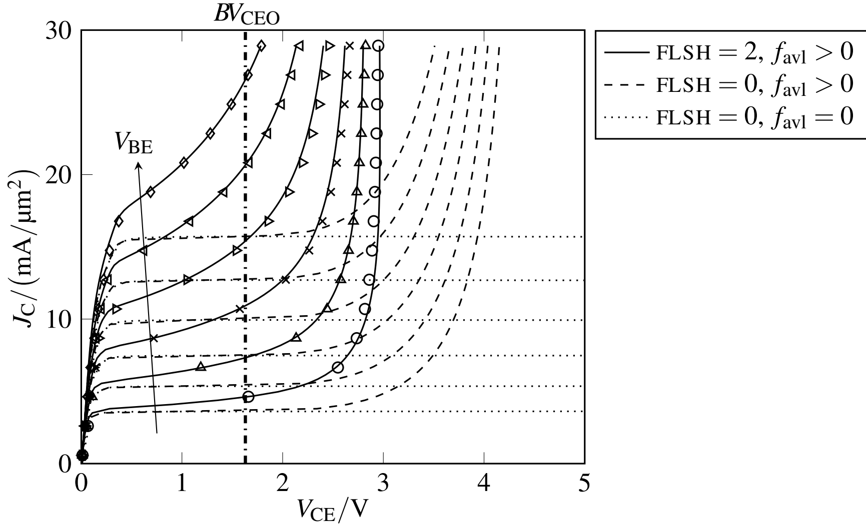

Figure 1.5: Output characteristics (forced I_C, sensed V_{CE}) with $V_{BE} = 0.86...0.96\,\text{V}$ in steps of $20\,\text{mV}$. Symbols: Measurement data. Lines: Simulation data. $b_{E0} = 0.12\,\mu\text{m}$, $l_{E0} = 2.65\,\mu\text{m}$. © IEEE [163]. © IEEE [166].

Self-heating and avalanche multiplication. Fig. 1.5 analyzes the impact of self-heating (SH) and avalanche multiplication (AVL) on output characteristics. The measured output characteristics shown in Fig. 1.5 have been obtained with high-frequency GSG probes by forcing I_C and sensing V_{CE} so as to capture the high-injection and strong avalanche regions while avoiding thermal runaway. Fig. 1.5 indicates that if output characteristics are measured with forced V_{BE}, the maximum quiescent V_{CE} can significantly exceed the open-base collector-emitter breakdown voltage BV_{CEO}. This demonstrates that breakdown voltages do not describe static voltages at which the transistor actually breaks, making the designation "breakdown" misleading. They are rather defined for very specific static bias conditions, i.e., BV_{CEO} is defined for an open base terminal, whereas BV_{CBO} is defined at very low injection levels. The simulated output characteristics with enabled self-heating (here FLSH = 2 [132]) and avalanche multiplication ($f_{avl} > 0$) have been obtained using HICUM/L2 with an avalanche current formulation that depends on the collector injection level [65, 73], yielding excellent agreement with measurement data. Fig. 1.5 demonstrates that at moderate to high V_{BE}, the positive feedback between self-heating and avalanche multiplication results in a limitation of the maximum attainable quiescent V_{CE}, so that the corresponding quiescent V_{CB} cannot achieve the low-injection limit BV_{CBO}. At very high V_{BE}, self-heating is the predominant phenomenon, leading to a significant J_C increase. These insights

concern the selection of the quiescent operating point. The real part of the optimum fundamental load impedance in class-A power amplifier operation, estimated according to load line theory as [29, 39]

$$\mathrm{Re}\{\underline{Z}_\mathrm{L}\} \approx \frac{V_\mathrm{max} - V_\mathrm{knee}}{I_\mathrm{max}}, \tag{1.4}$$

with the maximum current I_max and voltage V_max, and the knee voltage V_knee, is used to estimate the RF output power as

$$P_\mathrm{out,max} \approx \frac{1}{2}\left(\frac{I_\mathrm{max}}{2}\right)^2 \mathrm{Re}\{\underline{Z}_\mathrm{L}\} \approx \frac{1}{2}\left(\frac{I_\mathrm{max}}{2}\right)^2 \frac{V_\mathrm{max} - V_\mathrm{knee}}{I_\mathrm{max}}, \tag{1.5}$$

resulting in

$$P_\mathrm{out,max} \approx \frac{1}{8} I_\mathrm{max}(V_\mathrm{max} - V_\mathrm{knee}) \approx \frac{1}{4} I_\mathrm{max}(V_\mathrm{op} - V_\mathrm{knee}), \tag{1.6}$$

assuming linear voltage swings, i.e., $V_\mathrm{max} - V_\mathrm{knee} \approx 2(V_\mathrm{op} - V_\mathrm{knee})$. Thus (1.6) suggests that the quiescent $V_\mathrm{op} = V_\mathrm{CE}$ needs to be as high as possible to maximize $P_\mathrm{out,max}$, whereas Fig. 1.5 exemplifies that the range of practically relevant quiescent V_CE is restricted. In the RF stress tests of this thesis, SiGe HBTs are operated with quiescent $V_\mathrm{CE} > BV_\mathrm{CEO}$ before, but in proximity to, the considerable J_C increase induced by the positive feedback between self-heating and avalanche multiplication.

The dashed output characteristics in Fig. 1.5 represent the case where avalanche multiplication is turned on ($f_\mathrm{avl} > 0$) and self-heating is turned off ($\mathrm{FLSH} = 0$). Given the above rationale regarding dynamic self-heating (cf. Fig. 1.4 and (1.3)), these are the actual output characteristics "seen" by an RF signal with $f > 1\,\mathrm{GHz}$, assuming impact ionization to occur instantaneously. Hence, the small-signal output conductance valid for dynamic operation differs from the derivative of the static output characteristic in a specific quiescent operating point, as static characteristics include self-heating, which is significantly diminished in dynamic operation.

Moreover, as state-of-the-art SiGe HBTs achieve maximum RF performance at static power densities, which imply considerable self-heating, they need to be operated at high junction temperatures. Consequently, this thesis also reveals the electrothermal limits of static SiGe HBT operation as part of the comprehensive reliability studies.

Impact ionization is known to occur significantly faster than self-heating [81]. Also electrons, which are likely to collide with atoms within the BC space charge region, "gain much less energy than according to the maximum electric field" [146]. This is partially due to the small width of the E-field peak [146]. At present, no established theory or experimental verification exists regarding the activation time (or time constant) required for impact ionization in dynamic operation. Furthermore, previously

reported research, which specifically addresses impact ionization in bipolar transistors, is restricted to DC or (quasi-)static operation, e.g., forced-I_C, sensed-V_{CE} DC characterization [64], weak avalanche [139], strong avalanche [63], avalanche at different injection levels [65], review of different avalanche model formulations [32], bias-dependent instabilities [121, 124], investigation with a distributed transistor model [123].

Device reliability considerations in RF circuit design. The purpose of Fig. 1.6 is to illustrate RF device reliability considerations from an RF circuit designer's perspective. Therefore Fig. 1.6 depicts static measurements to experimentally determine static breakdown voltages, i.e., $J_C(V_{CE})|_{I_B=0}$ to determine BV_{CEO} (circles) and $J_C(V_{CE})|_{V_{BE}=0}$ to estimate BV_{CBO} (triangles). In particular the relation $J_C(V_{CE})|_{I_B=0}$ shows a significant increase for $V_{CE} > BV_{CEO}$ (circles). Values for BV_{CEO} and BV_{CBO}, which are typically provided by the foundry, are indicated as orientation in Fig. 1.6 by vertical dash-dotted lines.

The output characteristics in Fig. 1.6 measured with forced I_C and sensed V_{CE} at forced V_{BE} exhibit restricted maximum quiescent V_{CE} values due to the positive feedback between avalanche multiplication and self-heating.

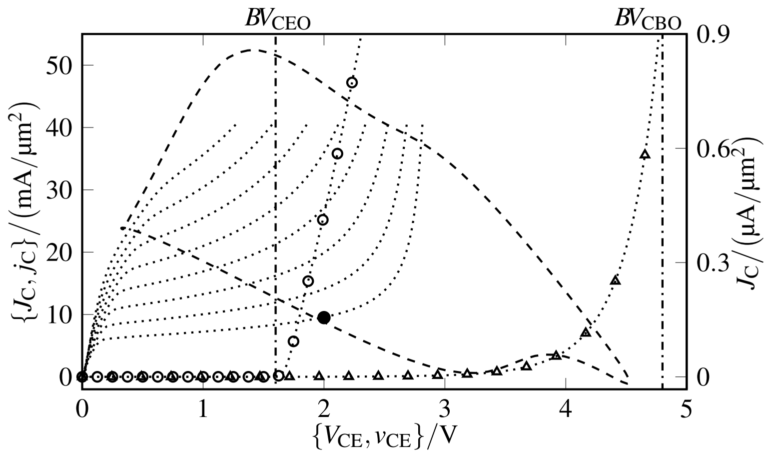

Figure 1.6: RF device reliability considerations. Triangles: measured $J_C(V_{CE})$ at $V_{BE} = 0$ (only curve belonging to right y-axis) to characterize $BV_{CBO} \approx 4.8\,\text{V}$ (indicated by vertical dash-dotted line). Circles: measured $J_C(V_{CE})$ at $I_B = 0$ to characterize $BV_{CEO} \approx 1.6\,\text{V}$ (indicated by vertical dash-dotted line). Dotted lines: measured output characteristics (forced I_C, sensed V_{CE}) with $V_{BE} = 0.9...1.04\,\text{V}$ in steps of $20\,\text{mV}$. Dashed line: simulated load ellipse with maximized $v_{CE}(t)$ swing applied in [161]. The quiescent operating point $(J_C, V_{CE}) = (9.5\,\text{mA}/\mu\text{m}^2, 2\,\text{V})$ of RF operation is marked by the dot. The data were obtained with a DUT with $b_{E0} = 0.12\,\mu\text{m}$, $l_{E0} = 5.15\,\mu\text{m}$. © IEEE [163].

The simulated load ellipse[2], i.e., $j_{\mathrm{C}}(t)$-$v_{\mathrm{CE}}(t)$, in Fig. 1.6 causes transient $v_{\mathrm{CE}}(t)$ swings far beyond BV_{CEO} up to $v_{\mathrm{CE}}(t)(\approx v_{\mathrm{CB}}(t)) \approx BV_{\mathrm{CBO}}$. The load ellipse results from a quiescent operating point $(J_{\mathrm{C}}, V_{\mathrm{CE}}) = (9.5\,\mathrm{mA/\mu m^2}, 2\,\mathrm{V})$ at elevated RF output power density and load conditions discussed in Sec. 3.4 [161]. The most conservative limit specified by foundries in PDKs is BV_{CEO}. However, the load ellipse in Fig. 1.6 is obtained with a quiescent $V_{\mathrm{CE}} > BV_{\mathrm{CEO}}$. DC stress tests previously performed in the literature (e.g., [96, 167]) indicate that a quiescent $V_{\mathrm{CE}} > BV_{\mathrm{CEO}}$ at different J_{C} causes only a low-injection base current increase.

The fundamental research question that remains to be answered concerns dynamic large-signal limits, i.e., the maximum output voltage amplitude or maximum allowed $j_{\mathrm{C}}(t)$-$v_{\mathrm{CE}}(t)$ trajectories. Conventional static stress tests are insufficient for the evaluation of reliability concerns, which arise from dynamic large-signal HBT operation, such as exemplified in Fig. 1.6, because transient $j_{\mathrm{C}}(t)$-$v_{\mathrm{CE}}(t)$ can reach values much larger than the maximum DC-measured J_{C}-V_{CE}. The reason is that static breakdown phenomena, e.g., self-heating in Fig. 1.4 and (1.3), are diminished in dynamic transistor operation, thus widening the RF voltage and current density range. Consequently, the characterization of RF operating limits requires RF stress tests. RF trajectories $j_{\mathrm{C}}(t)$-$v_{\mathrm{CE}}(t)$ are an attribute of dynamic large-signal transistor operation and thus expose the transistor to a type of stress that is different from classic DC stress. This makes RF stress tests indispensable for understanding RF operating limits.

Literature and workshops. At the time of submission, several parts of the results of this thesis have been published by the author as regular papers [161, 165] and as an invited paper [163] in the proceedings of the *IEEE BiCMOS Comp. Semicond. Integr. Circuits Technol. Symp.* In addition, several parts of the results have been published in the proceedings of the *IEEE/MTT-S Int. Microw. Symp.* [162, 164]. The journal article [166], published in the *IEEE Trans. Device Mater. Rel.*, brings all previous results into a single coherent context and extends the scope of data analysis. Moreover, selected results have been presented at several workshops [155] - [160], including one at the *2022 IEEE/MTT-S Int. Microw. Symp.* Selected results have also been presented to Infineon Technologies, Rohde & Schwarz and Globalfoundries.

[2] Note that the notation x-y used throughout this thesis denotes a pair of current density-voltage values. Thus $j_{\mathrm{C}}(t)$-$v_{\mathrm{CE}}(t)$ denotes a pair of transient values, whereas J_{C}-V_{CE} denotes a pair of quiescent values.

Relative deviation. The relative deviation as a percentage of an observable is investigated with respect to the initial measurement performed prior to a stress test, i.e., at $t_{\text{stress}} = 0$. The relative degradation of a quantity Q is denoted and defined as

$$\delta\left(Q\right) = \frac{Q(t_{\text{stress}}) - Q(t_{\text{stress}} = 0)}{|Q(t_{\text{stress}} = 0)|}. \tag{1.7}$$

Area-normalized logarithmic RF output power. To define comparable RF stress conditions for SiGe HBTs with varying geometries and across different technologies, the quantity[3]

$$\rho_{\text{L,del}} = 10\log_{10}\left(\frac{P_{\text{L,del}}}{A_{\text{E0}}} \bigg/ \frac{\text{mW}}{\mu\text{m}^2}\right) \tag{1.8}$$

is introduced to refer to logarithmic RF output power *density* instead of RF output power in dBm.

Length-normalized logarithmic RF output power. Typically, MOSFET quantities are normalized to the effective gate width $W_{\text{G,eff}} = n_{\text{G}} W_{\text{G}}$ with W_{G} as the gate width and n_{G} as the number of gate fingers. The power delivered to the load $P_{\text{L,del}}$ by a MOSFET is thus normalized to $W_{\text{G,eff}}$, and the normalized logarithmic RF output power $\sigma_{\text{L,del}}$ is introduced

$$\sigma_{\text{L,del}} = 10\log_{10}\left(\frac{P_{\text{L,del}}}{W_{\text{G,eff}}} \bigg/ \frac{\text{mW}}{\mu\text{m}}\right). \tag{1.9}$$

To have comparable quantity for HBTs, the RF output power is normalized to the total emitter length, resulting in the logarithmic quantity[4]

$$\sigma_{\text{L,del}} = 10\log_{10}\left(\frac{P_{\text{L,del}}}{l_{\text{E0}}} \bigg/ \frac{\text{mW}}{\mu\text{m}}\right). \tag{1.10}$$

Plots of time-dependent degradation. The line specifications of stress test plots, which show periodic measurements of a quantity in selected bias points versus cumulative stress time t_{stress}, are given in Tab. 1.1.

Table 1.1: Line specifications of plots showing periodic measurements of a quantity versus cumulative stress time t_{stress} in selected bias points.

line	purpose
solid, vertical	re-calibration & change of stress conditions
dash-dotted, vertical	re-calibration & no change of stress conditions

[3] Note that A_{E0} in (1.8) denotes the *total* emitter area of all emitter fingers, i.e., of all $N_x = 4$ HBTs in Ch. 6. In Ch. 2-5 and 7, single-emitter HBTs are investigated.

[4] Note that l_{E0} in (1.10) denotes the *total* emitter length of all emitter fingers, i.e., of all $N_x = 4$ HBTs in Ch. 6. In Ch. 2-5 and 7, single-emitter HBTs are investigated.

Conventions and notations. Note the following points:

- All stress tests with HBTs have been carried out at a chuck/die back-side temperature $T_B = 298\,K$. The only stress tests at elevated temperatures are the electromigration tests conducted on the backend-of-line detailed in Sec. 2.5. Throughout this thesis, if not stated otherwise, $T_B = 298\,K$.
- All stress tests in this thesis have been performed with DUTs in common-emitter (common-source) configuration embedded in GSG layouts, as this is the most frequently used (standard) configuration for device characterization and investigations at the semiconductor device level.
- Throughout this work, unless stated otherwise, degradation refers to phenomena beyond an increase of the DC base current I_B.
- The designations power delivered to the load and RF output power are used interchangeably. Both refer to the power $P_{L,del}$ at the DUT output reference plane (see Fig. 3.1 and related discussion).
- The designations RF signal trajectories, RF waveforms, load ellipse are used interchangeably and refer to the transient output current density against transient output voltage, i.e., $j_C(t)$ versus $v_{CE}(t)$ for an HBT.
- The SiGe HBT technology investigated in Ch. 2 - Ch. 6 is IHP's SG13G2. Only the comparative RF reliability study in Ch. 7 investigates different technologies: Infineon's SiGe HBT technology B11HFC, Teledyne's InP HBT technology TSC250, and Globalfoundries' MOSFET technology 22FDX.
- In certain plots depicting power sweep measurements versus simulations, e.g., in Fig. 3.15, the two columns describe two different power sweeps with different load conditions, i.e., a, c, e belong together and describe the first power sweep, whereas b, d, f describe the second power sweep.
- In plots depicting RF stress conditions, e.g., in Fig. 6.6, 7.13 or 7.19, all power sweeps belong to the same load conditions. These plots depict area-normalized and length-normalized RF output powers and currents.
- Plots depicting *simulated* load ellipses superimposed on *simulated* output characteristics also contain *measurements* of static HBT breakdown voltages BV_{CEO} and BV_{CBO}, e.g., Fig. 6.6d and e, or Fig. 7.13d and e, or breakdown experiments, e.g., Fig. 7.18e and f. These measurement data are shown as orientation. Note that low-injection limits, e.g., BV_{CBO} for SiGe HBTs, or BV_{CEO} and BV_{CBO} for InP HBTs, always belong to the right y-axis, whereas all other data belong to the left y-axis.